Solid Freeform Fabrication 2022: Proceedings of the 33rd Annual International Solid Freeform Fabrication Symposium – An Additive Manufacturing Conference
Reviewed Paper

KEY PROCESS VARIABLE (KPV) VARIATIONS AND THEIR IMPACT ON DEFECT STRUCTURE AND TENSILE BEHAVIOR OF L-PBF Ti-6Al-4V

Mohammad Salman Yasin, Arash Soltani-Tehrani, Arun Poudel, Shuai Shao, Nima Shamsaei*

National Center for Additive Manufacturing Excellence (NCAME), Auburn University, Auburn, AL 36849, USA
Department of Mechanical Engineering, Auburn University, Auburn, AL 36849, USA
* Corresponding author: shamsaei@auburn.edu

Abstract

The process variables used in laser powder bed fusion (L-PBF) influence the defect formation in fabricated parts. However, key process variables (KPVs) such as laser power, laser speed, and hatch distance may drift within their tolerances during service between calibrations. These variations can result in different defect contents in parts and, consequently, different mechanical properties. Therefore, this study investigates the effects of KPV drift on the porosity and tensile behavior of L-PBF Ti-6Al-4V. According to the original equipment manufacturer, EOS, the laser power and hatch distance were altered by ± 4% and ± 2.4%, respectively, to emulate the actual drift in KPVs. Porosity analysis and hardness tests on L-PBF Ti-6Al-4V parts showed no significant change. In addition, tensile tests illustrated no general trend for different KPV drift variations.

Introduction

Metal additive manufacturing (AM) is gaining popularity in aviation, automotive, and biomedical industries due to the possibility of fabricating monolithic parts with great geometrical complexity for a wide range of materials. With the exponential growth of AM in the manufacturing market, laser powder bed fusion (L-PBF) has become one of the most widely used AM processes [1]. However, to be considered a viable alternative to the conventional manufacturing processes (such as casting and forging), process variables are usually needed to be optimized for different material systems due to the dependency of mechanical properties on process-induced defects and microstructure [2–6].

More than 100 process variables are involved in most commercial L-PBF systems. In most cases, however, only the KPVs such as laser power, laser speed, hatch distance, and layer thickness are adjusted during the process optimization for any given material since they correlate well with the energy input and, consequently, the porosity formation and mechanical properties [7]. However, even with the optimized process variables, these parts are not always consistent due to the multiple physical phenomena occurring during the fabrication process [8].

To understand the different physical phenomena, research has been focused on the uncertainty in the L-PBF process variables and their impact on material behavior. With the exception of stripe width [7,9], process variables such as laser power [8,10–15], laser speed [10–14,16], hatch distance [11,14,17], type of inert gas used [18], build plate temperature [19], powder particle size distribution [20–23] part volume [24–26], surface conditions [27] are known to

influence defect formation and resultant mechanical behavior. While these studies established process variable effect on defect formation using larger parametric variations, the impact of machine tolerances (smaller variation in KPV) or KPV drift on resulting defect content, and mechanical behavior was not explored.

The current study assesses the impact of key process variables (KPV) drift on the defect formation and mechanical response in an EOS M290 L-PBF machine using Ti-6Al-4V (Ti-64) powder. During fabrication, the default process variables were based on the parameter set known as 'Ti64_Performance 1.0'. The process drift in laser power and hatch distance were imitated by changing them by ± 4% and ± 2.4% from the default value, respectively, which were tolerance bands specified by EOS original equipment manufacturer (OEM). In the following sections, a detailed experimental program and results and discussion will be presented.

Experimental Procedure

Witness coupons and round bar specimens were fabricated using an EOS M290 (EOS GmbH, Germany) L-PBF machine in the center region of the build plate with plasma atomized Ti-64 powder, supplied by AP&C, a GE Additive company. The coupons/specimens were fabricated in multiple builds from virgin/unused Ti-64 powder. After fabrication, the witness coupons were removed from the build plate, and the specimens were stress relieved on the build plate at 700° C in an argon atmosphere for an hour and then furnace-cooled to room temperature. The round bar specimens (of 10 mm in diameter and 100 mm in height) were machined to tensile specimens according to ASTM E8M [28]. The geometry of the witness coupon and machined tensile specimen can be seen in Figure 1.

To study the KPV drift in the L-PBF system, only laser power and hatch distance were varied based on the recommendation from EOS. The combined effect of different process variables is usually shown using the energy density, where the energy density is proportional to the laser power and inversely proportional to the hatch distance. In the current study, KPV drift conditions where concurrent changes in both laser power and hatch distance may lead to a cancellation effect, were not considered. A total of seven KPV drift conditions (as shown in Table 1) were thus considered for the experimental matrix. X-ray computed tomography (XCT) was conducted using a Zeiss Xradia 620 Versa to obtain the porosity information within the witness coupons. 140kV voltage and 150µA current were used to capture the defects with a voxel size of 5 µm. The X-ray projections were reconstructed into 3D volume information via Scout and Reconstruct, ImageJ, and Dragonfly software [29,30].

Additionally, the witness coupons were used to conduct hardness testing using a Rockwell hardness tester (Leco LCR500) in accordance with ASTM E18-20 [31]. The specimens were polished using sandpaper before the indentation test was conducted. At least eight indentations were made on the rectangular part of the witness coupon using a Rockwell C setup. The uniaxial tensile testing of the machined specimens was conducted at ambient temperature in an MTS landmark servo-hydraulic testing machine equipped with a 100 kN load cell. An extensometer was used to record the strain in the gage section. At least two specimens were tested for each KPV variation condition to obtain tensile properties.

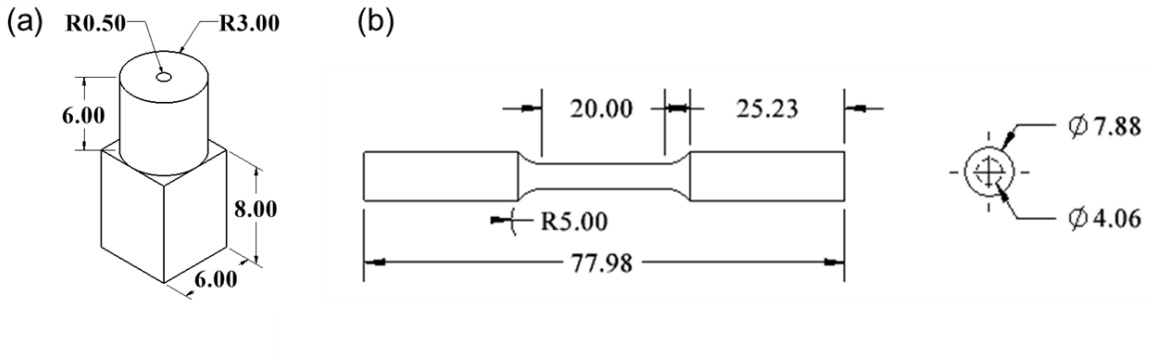

Figure 1: (a) The geometry of witness coupons used for XCT and hardness measurement, and (b) the geometry of machined tensile specimens based on ASTM E8M. All dimensions are in mm

Table 1: Designations used for coupon/specimen fabrication of different KPV drift conditions and related process variables

Condition	Laser Power (W)	Hatch Distance (µm)	Laser Speed (mm/s)	Layer Thickness (µm)
P+h-	291.2	143.4		
P+h0	291.2	140.0		
P0h+	280.0	143.4		
P0h0	280.0	140.0	1200.0	30.0
P0h-	280.0	136.6		
P-h0	268.8	140.0		
P-h+	268.8	143.4		

Results and Discussion

XCT scans are conducted on the cylindrical part of the witness coupons. It should be noted that defects with equivalent spherical diameter (defined as the diameter of a sphere of equivalent volume as the defect) less than 15 µm are not considered during the analysis to avoid false-positive detection of defects. The summary of the quantitative porosity inspection can be seen in Table 2, and the defect distribution within the coupons is displayed in Figure 2 with respect to the equivalent-volume sphere diameter. Evaluation of the different KPV condition coupons reveals that the porosity of the fabricated coupons has a similar response to the changes in laser power and hatch distance. However, for all inspected coupons, there is not a significant change in the porosity since there was only a slight variation in the energy density for all KPVs. As shown in Figure 2, equivalent-volume sphere diameter distribution is found to be similar in most cases.

Table 2: Quantitative levels of porosity evaluated from the XCT coupons fabricated at different KPV condition

Condition	P+h-	P+h0	P0h+	P0h0	P0h-	P-h0	P-h+
Energy Density (J/mm^3)	59.20	57.78	56.92	55.56	54.25	53.33	52.08
Porosity (%)	0.0002	0.0004	0.0003	0.0003	0.0004	0.0004	0.0009

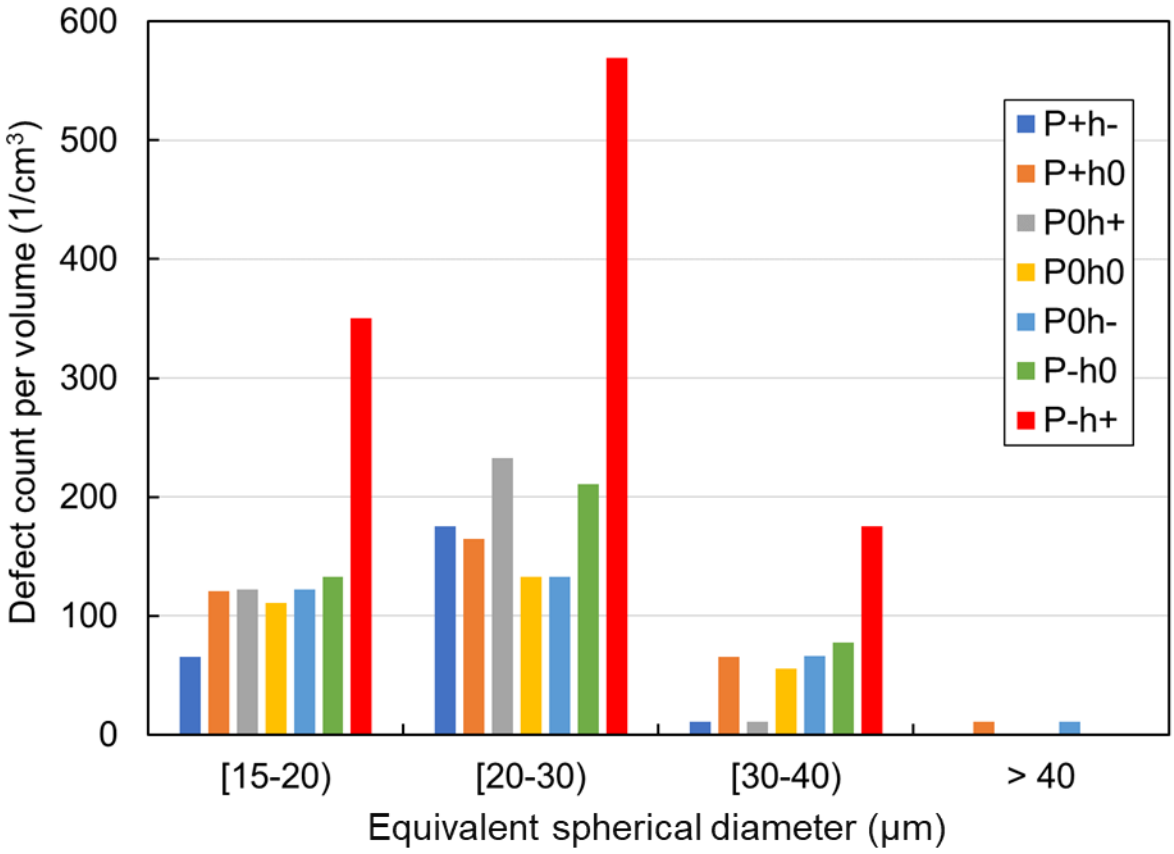

Figure 2: Comparative column chart of equivalent-volume sphere diameter distribution in witness coupons for different KPV conditions

The summary of Rockwell hardness test results is shown in Figure 3 as a box and whisker plot. The mean and range of hardness measurements is similar in all seven cases. To identify the variation of the KPV and their impact on the hardness, a one-way analysis of variance (ANOVA) has been conducted using the SAS software. The summary of the ANOVA analysis can be seen in Table 3. The ANOVA analysis looks into the variance within the different groups and finds if the variations are significantly different [32]. Since the p-value was larger than the critical value of 0.05, it can be estimated that there is no significant difference in hardness for different KPV conditions.

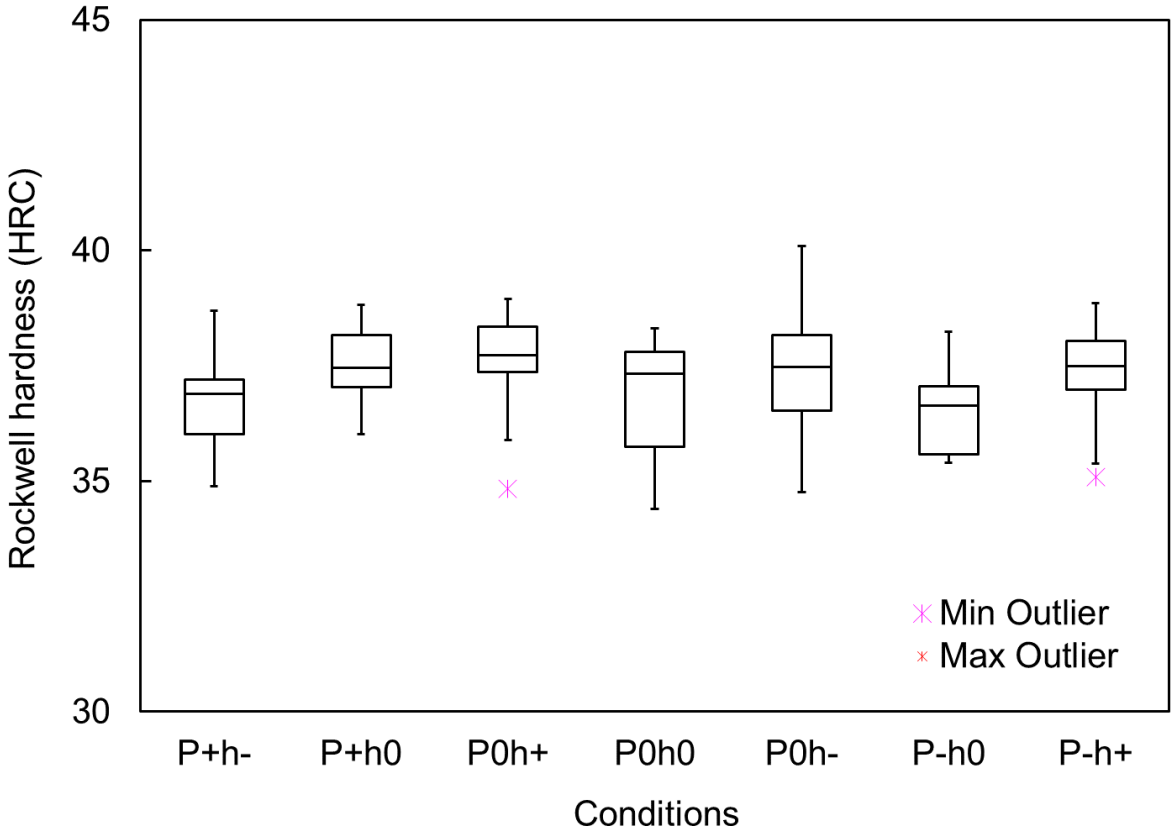

Figure 3: Rockwell hardness (C-scale) test result of different KPV conditions

Table 3: One-way ANOVA for hardness within different groups

Source of Variation	Degree of Freedom	Sum of Squares	Mean Square	F Value	p-value
Between groups	6	9.43	1.57	1.01	0.43
Within groups	49	76.51	1.56		
Corrected Total	55	85.95			

The summary of the uniaxial tensile test results is shown in Figure 4 in terms of yield strength (Y), ultimate tensile strength (UTS), and elongation to failure (El%). Similar to the hardness results, the tensile properties of the fabricated specimens do not vary significantly. Although there is a slight difference in strength, the material's ductility remained almost the same

for different KPV conditions. The results are consistent with the ones found for porosity and hardness.

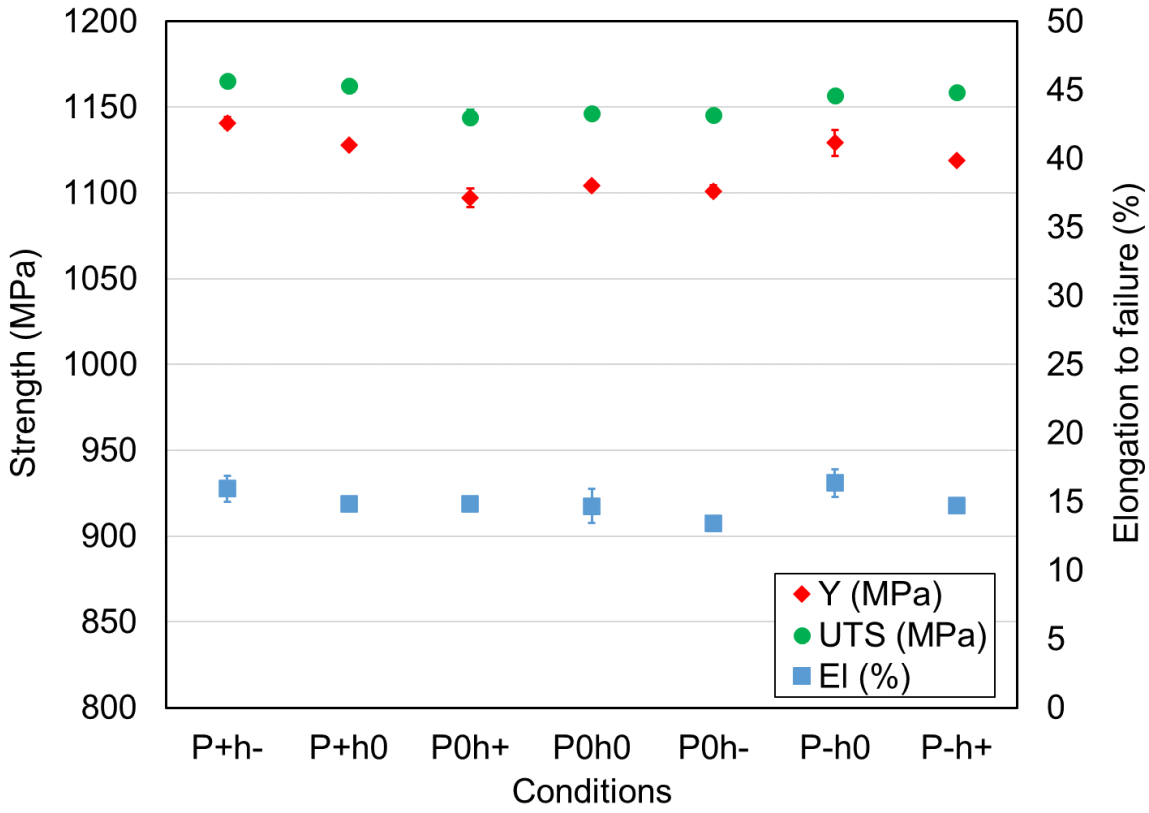

Figure 4: A summary of tensile properties for different KPV conditions. The error bars indicate the variability of observations for different conditions

Conclusions

The present study explored the impact of KPV drift within the tolerance bands on porosity and the resultant mechanical behavior of L-PBF Ti-64. The major conclusions from this study are as follows:

- Defect formation is influenced in a similar manner for both laser power and hatch distance in L-PBF Ti-64.
- Porosity is somewhat comparable for all the KPV conditions.
- No general trends in hardness or tensile properties are observed due to the KPV drift during fabrication.
- The one-way ANOVA does not show a significant impact of KPVs on hardness results.

Acknowledgments

This material is based upon the work partially supported by National Science Foundation (NSF) under grant # 1919818 and Federal Aviation Administration (FAA) under grant # FAA-12-C-AM-AU-A2.

References

[1] J.P. Oliveira, A.D. LaLonde, J. Ma, Processing parameters in laser powder bed fusion metal additive manufacturing, Mater. Des. 193 (2020) 108762. https://doi.org/10.1016/j.matdes.2020.108762.

[2] K. Dietrich, J. Diller, S. Dubiez-Le Goff, D. Bauer, P. Forêt, G. Witt, The influence of oxygen on the chemical composition and mechanical properties of Ti-6Al-4V during laser powder bed fusion (L-PBF), Addit. Manuf. 32 (2020) 100980. https://doi.org/10.1016/j.addma.2019.100980.

[3] H. Shipley, D. McDonnell, M. Culleton, R. Coull, R. Lupoi, G. O'Donnell, D. Trimble, Optimisation of process parameters to address fundamental challenges during selective laser melting of Ti-6Al-4V: A review, Int. J. Mach. Tools Manuf. 128 (2018) 1–20. https://doi.org/10.1016/j.ijmachtools.2018.01.003.

[4] A. Poudel, A. Soltani-Tehrani, S. Shao, N. Shamsaei, Effect of powder characteristics on tensile properties of additively manufactured 17-4 PH stainless steel, 2021 Int. Solid Free. Fabr. Symp. (2021).

[5] A. Poudel, N. Shamsaei, S. Shao, Linear elastic finite element calculations of short cracks initiated from the defects : effect of defect shape and size, 2021 Int. Solid Free. Fabr. Symp. (2021) 915–922.

[6] M.S. Yasin, A. Soltani-Tehrani, S. Shao, M. Haghshenas, N. Shamsaei, A Comparative Study on Fatigue Performance of Various Additively Manufactured Titanium Alloys, Procedia Struct. Integr. 38 (2022) 519–525.

[7] C. Högman, The effect of stripe width, stripe overlap, gas flow, and scan angle on process stability in Laser Powder Bed Fusion (L-PBF), Karlstads University, 2021.

[8] T. Moges, W. Yan, S. Lin, G. Ameta, J. Fox, P. Witherell, Quantifying uncertainty in laser powder bed fusion additive manufacturing models and simulations, in: 2018 Int. Solid Free. Fabr. Symp., University of Texas at Austin, 2018.

[9] A. Soltani-Tehrani, M.S. Yasin, S. Shao, N. Shamsaei, Effects of Stripe Width on the Porosity and Mechanical Performance of Additively Manufactured Ti-6Al-4V Parts, in: 2021 Int. Solid Free. Fabr. Symp., University of Texas at Austin, 2021.

[10] Z. Gan, O.L. Kafka, N. Parab, C. Zhao, L. Fang, O. Heinonen, T. Sun, W.K. Liu, Universal scaling laws of keyhole stability and porosity in 3D printing of metals, Nat. Commun. 12 (2021). https://doi.org/10.1038/s41467-021-22704-0.

[11] A. du Plessis, Effects of process parameters on porosity in laser powder bed fusion revealed by X-ray tomography, Addit. Manuf. 30 (2019) 100871. https://doi.org/10.1016/j.addma.2019.100871.

[12] H. Gong, K. Rafi, H. Gu, T. Starr, B. Stucker, Analysis of defect generation in Ti-6Al-4V

parts made using powder bed fusion additive manufacturing processes, Addit. Manuf. 1 (2014) 87–98. https://doi.org/10.1016/j.addma.2014.08.002.

[13] R. Cunningham, C. Zhao, N. Parab, C. Kantzos, J. Pauza, K. Fezzaa, T. Sun, A.D. Rollett, Keyhole threshold and morphology in laser melting revealed by ultrahigh-speed x-ray imaging, Science (80-.). 363 (2019) 849–852. https://doi.org/10.1126/science.aav4687.

[14] J. Kluczyński, L. Śnieżek, K. Grzelak, J. Mierzyński, The influence of exposure energy density on porosity and microhardness of the SLM additive manufactured elements, Materials (Basel). 11 (2018) 2304.

[15] M. Tang, P.C. Pistorius, J.L. Beuth, P. Chris Pistorius, Prediction of lack-of-fusion porosity for powder bed fusion, Addit. Manuf. 14 (2017) 39–48. https://doi.org/10.1016/j.addma.2016.12.001.

[16] T. Montalbano, B.N. Briggs, J.L. Waterman, S. Nimer, C. Peitsch, J. Sopcisak, D. Trigg, S. Storck, Uncovering the coupled impact of defect morphology and microstructure on the tensile behavior of Ti-6Al-4V fabricated via laser powder bed fusion, J. Mater. Process. Technol. 294 (2021) 117113. https://doi.org/10.1016/j.jmatprotec.2021.117113.

[17] L. Sheridan, O.E. Scott-Emuakpor, T. George, J.E. Gockel, Relating porosity to fatigue failure in additively manufactured alloy 718, Mater. Sci. Eng. A. 727 (2018) 170–176.

[18] C. Pauzon, P. Forêt, E. Hryha, T. Arunprasad, L. Nyborg, Argon-helium mixtures as Laser-Powder Bed Fusion atmospheres: Towards increased build rate of Ti-6Al-4V, J. Mater. Process. Technol. 279 (2020) 116555. https://doi.org/10.1016/j.jmatprotec.2019.116555.

[19] P.D. Nezhadfar, A. Soltani-Tehrani, N. Shamsaei, Effect of Preheating Build Platform on Microstructure and Mechanical Properties of Additively Manufactured 316L Stainless Steel, in: Proc. 30th Annu. Int. Solid Free. Fabr. Symp. Addit. Manuf. Conf., 2019: pp. 415–425.

[20] A. Soltani-Tehrani, M.S. Yasin, M. Habibnejad, M. Haghshenas, N. Shamsaei, Effects of Powder Particle Size on Fatigue Performance of Laser Powder-Bed Fused Ti-6Al-4V, in: Fatigue Des. 2021, 2021.

[21] Z.M. Jian, G.A. Qian, D.S. Paolino, A. Tridello, F. Berto, Y.S. Hong, Crack initiation behavior and fatigue performance up to very-high-cycle regime of AlSi10Mg fabricated by selective laser melting with two powder sizes, Int. J. Fatigue. 143 (2021) 106013.

[22] A. Soltani-Tehrani, M. Habibnejad-Korayem, S. Shao, M. Haghshenas, N. Shamsaei, Ti-6Al-4V powder characteristics in laser powder bed fusion: The effect on tensile and fatigue behavior, Addit. Manuf. 51 (2022) 102584.

[23] A. Soltani-Tehrani, M.S. Yasin, S. Shao, N. Shamsasei, Effects of Powder Reuse and Spatial Location Dependency on the Powder Characteristics and Defect Structure of Additively Manufactured Ti-6Al-4V Parts, in: 2021 Int. Solid Free. Fabr. Symp., University of Texas at Austin, 2021.

[24] A. Leicht, C. Pauzon, M. Rashidi, U. Klement, L. Nyborg, E. Hryha, Effect of part thickness on the microstructure and tensile properties of 316L parts produced by laser powder bed fusion, Adv. Ind. Manuf. Eng. 2 (2021) 100037. https://doi.org/https://doi.org/10.1016/j.aime.2021.100037.

[25] R. Shrestha, N. Shamsaei, M. Seifi, N. Phan, An investigation into specimen property to part performance relationships for laser beam powder bed fusion additive manufacturing, Addit. Manuf. 29 (2019) 100807. https://doi.org/https://doi.org/10.1016/j.addma.2019.100807.

[26] A. Soltani-Tehrani, R. Shrestha, N. Phan, M. Seifi, N. Shamsaei, Establishing Specimen Property to Part Performance Relationships for Laser Beam Powder Bed Fusion Additive Manufacturing, Int. J. Fatigue. (2021).

[27] S. Lee, N. Ahmad, K. Corriveau, C. Himel, D.F. Silva, N. Shamsaei, Bending properties of additively manufactured commercially pure titanium (CPTi) limited contact dynamic compression plate (LC-DCP) constructs: Effect of surface treatment, J. Mech. Behav. Biomed. Mater. 126 (2022) 105042.

[28] ASTM International, E8/E8M Standard Test Methods for Tension Testing of Metallic Materials, West Conshohocken, PA; ASTM Int. (2016). https://doi.org/https://doi.org/10.1520/E0008_E0008M-13.

[29] C.A. Schneider, W.S. Rasband, K.W. Eliceiri, NIH Image to ImageJ: 25 years of image analysis, Nat. Methods. 9 (2012) 671–675. https://doi.org/10.1038/nmeth.2089.

[30] Dragonfly 2020.2 [Computer software], 2020. http://www.theobjects.com/dragonfly.

[31] ASTM International, Standard Test Methods for Rockwell Hardness of Metallic Materials, 2021.

[32] A. Cuevas, M. Febrero, R. Fraiman, An anova test for functional data, Comput. Stat. Data Anal. 47 (2004) 111–122.